Available online at www.sciencedirect.com
SCIENCE DIRECT®
Icarus 182 (2006) 383–395
ICARUS
www.elsevier.com/locate/icarus

# Numerical interpretation of high-altitude photoelectron observations

Michael W. Liemohn [a,*], R.A. Frahm [b], J.D. Winningham [b], Y. Ma [a], S. Barabash [c], R. Lundin [c], J.U. Kozyra [a], A.F. Nagy [a], S.M. Bougher [a], J. Bell [a], D. Brain [d], D. Mitchell [d], J. Luhmann [d], M. Holmström [c], H. Andersson [c], M. Yamauchi [c], A. Grigoriev [c], S. McKenna-Lawler [e], J.R. Sharber [f], J.R. Scherrer [f], S.J. Jeffers [f], A.J. Coates [g], D.R. Linder [g], D.O. Kataria [g], E. Kallio [h], H. Koskinen [h,1], T. Säles [h], P. Riihelä [h], W. Schmidt [h], E. Roelof [i], D. Williams [i], S. Livi [i], C.C. Curtis [j], K.C. Hsieh [j], B.R. Sandel [j], M. Grande [k], M. Carter [k], J.-A. Sauvaud [l], A. Fedorov [l], J.-J. Thocaven [l], S. Orsini [m], R. Cerulli-Irelli [m], M. Maggi [m], P. Wurz [n], P. Bochsler [n], N. Krupp [o], J. Woch [o], M. Fränz [o], K. Asamura [p], C. Dierker [q]

[a] *Department of Atmospheric, Oceanic, and Space Sciences, University of Michigan, Ann Arbor, MI 48109-2143, USA*
[b] *Southwest Research Institute, San Antonio, TX, USA*
[c] *Swedish Institute of Space Physics, Box 812, S-98 128, Kiruna, Sweden*
[d] *Space Sciences Laboratory, University of California, Berkeley, CA, USA*
[e] *Space Technology Ireland, National University of Ireland, Maynooth, Co. Kildare, Ireland*
[f] *Southwest Research Institute, San Antonio, TX 7228-0510, USA*
[g] *Mullard Space Science Laboratory, University College London, Surrey RH5 6NT, UK*
[h] *Finnish Meteorological Institute, Box 503, FIN-00101 Helsinki, Finland*
[i] *Applied Physics Laboratory, Johns Hopkins University, Laurel, MD 20723-6099, USA*
[j] *University of Arizona, Tucson, AZ 85721, USA*
[k] *Rutherford Appleton Laboratory, Chilton, Didcot, Oxfordshire OX11 0QX, UK*
[l] *Centre d'Etude Spatiale des Rayonnements, BP-4346, F-31028 Toulouse, France*
[m] *Istituto di Fisica dello Spazio Interplanetari, I-00133 Rome, Italy*
[n] *Physikalisches Institut, University of Bern, CH-3012 Bern, Switzerland*
[o] *Max-Planck-Institut für Aeronomie, D-37191 Katlenburg-Lindau, Germany*
[p] *Institute of Space and Astronautical Science, 3-1-1 Yoshinodai, Sagamichara, Japan*
[q] *Technical University of Braunschweig, Hans-Sommer-Strasse 66, D-38106 Braunschweig, Germany*

Received 14 April 2005; revised 22 August 2005

Available online 30 January 2006

**Abstract**

The Electron Spectrometer (ELS) instrument of the ASPERA-3 package on the Mars Express satellite has recorded photoelectron energy spectra up to apoapsis (∼10,000 km altitude). The characteristic photoelectron shape of the spectrum is sometimes seen well above the ionosphere in the evening sector across a wide range of near-equatorial latitudes. Two numerical models are used to analyze the characteristics of these high-altitude photoelectrons. The first is a global, multi-species MHD code that produces a 3-D representation of the magnetic field and bulk plasma parameters around Mars. It is used here to examine the possibility of magnetic connectivity between the high-altitude flanks of the martian ionosheath and the subsolar ionosphere. It is shown that some field lines in this region are draped interplanetary magnetic lines while others are open field lines (connected to both the IMF and the crustal magnetic field sources). The second model is a kinetic electron transport model that calculates the electron velocity space distribution along a selected, non-uniform, magnetic field line. It is used here to simulate the high-altitude ELS measurements. It is shown that the photoelectrons are essentially confined to the source cone, as governed by magnetic field inhomogeneity along the field line. Reasonable agreement is shown between the data and the model results, and a method is demonstrated for inferring properties of

* Corresponding author. Fax: +1 734 647 3083.
*E-mail address:* liemohn@umich.edu (M.W. Liemohn).

[1] Also at the Department of Physical Sciences, University of Helsinki, P.O. Box 64, FIN-00014 Helsinki, Finland.

0019-1035/$ – see front matter © 2005 Elsevier Inc. All rights reserved.
doi:10.1016/j.icarus.2005.10.036

the local and photoelectron source region magnetic field from the ELS measurements. Specifically, the number of sectors in which photoelectrons are measured is a function of the magnetic field intensity ratio and the field's angle with respect to the detector plane. In addition, the sector of the photoelectron flux peak is a function of the magnetic field azimuthal angle in the detector plane.
© 2005 Elsevier Inc. All rights reserved.

*Keywords:* Mars; Magnetospheres; Ionospheres; Magnetic fields

## 1. Introduction

Frahm et al. (2006) (this issue) report the observation of atmospheric photoelectrons far above the martian ionosphere. These measurements, made by the ASPERA-3 instrument package (Barabash et al., 2004) onboard the Mars Express satellite (Chicarro et al., 2004), are the first of their kind. The high spectral resolution of the ELS component of ASPERA-3 allows for the detection of the primary production peaks, which are created due to atmospheric ionization by the HeII 30.4 nm line. These photoelectrons are sometimes observed all the way up to apoapsis (∼10,000 km altitude) behind the terminator plane. This is well above the photoelectron boundary defined by the Mars Global Surveyor MAG/ER measurements (Mitchell et al., 2000, 2001). Most of the observations were obtained on the dusk side of Mars, but this is probably an orbital bias. Photoelectrons are recorded regularly, either in sporadic patches along the orbit or sometimes continuously for several tens of degrees of latitude and thousands of kilometers in altitude variation.

The question of how these atmospheric photoelectrons got there is still open to debate. The equally important question of what can be learned from their existence in the high-altitude flanks of the martian ionosheath is also unanswered. This study addresses these questions with the aid of two numerical models. The first is a magnetohydrodynamic (MHD) code that simulates the global magnetic topology around Mars (Ma et al., 2004). The second is a kinetic transport model that calculates the velocity space distribution of the photoelectrons along a chosen magnetic field line (Liemohn et al., 2003). After a presentation of several sample observations of the high-altitude photoelectrons, results from the two computational tools are presented to examine the possible origin of these particles. It is shown how these results can be used to deduce information about the local magnetic field direction and the magnetic field ratio between the source region and the observation point. This is a critical deduction because there is no magnetometer on Mars Express. A comparison of the modeled and deduced magnetic field parameters can be used to deduce the source region of the photoelectrons as well as the magnetic topology of the field line on which they traveled (that is, draped across the dayside or connected to the crustal field sources).

## 2. Observations

The Mars Express satellite reached its destination in December of 2003, and entered into a highly elliptical orbit around the planet. Apoapsis is above 10,000 km altitude while periapsis is near 250 km altitude (Chicarro et al., 2004). Therefore, during every orbit, the satellite usually pass as through regions of unperturbed solar wind, the magnetosheath, and the ionosphere.

The Analyzer of Space Plasmas and Energetic Atoms (ASPERA-3) experiment onboard Mars Express is a collection of detectors designed to study the solar wind–atmosphere interaction at Mars (Barabash et al., 2004). Of particular interest in this regard is the electron spectrometer (ELS). It consists of a collimator followed by a standard top-hat electrostatic analyzer, with a micro channel plate and anode ring below this. The anode is divided into 16 sectors of 22.5°, making the field of view 360° times the 4° collimator window. The energy range extends from below an electron volt to ∼20 keV, with a $\Delta E/E$ of 0.08.

Since Mars Express does not have an onboard magnetometer, the magnitude and direction of the magnetic field are unknown and, therefore, it is not known how to convert between sector angle and pitch angle ($\alpha$). Despite this, it is known that the sampled pitch angle range is centered about 90° (locally mirroring electrons) and that it extends over some $\Delta\alpha$ in each direction away from $\alpha = 90°$. If the magnetic field vector is perpendicular to the ELS anode plane, then only locally mirroring electrons will be measured. However, if the magnetic field vector is in the plane of the anode, then the entire 180° pitch angle range will be observed. (Note that because the anode is a ring, each pitch angle within the sampled range is measured twice.)

Let us now discuss the high-altitude photoelectron observations made by the ASPERA-3 ELS instrument. Fig. 1 presents the electron differential number flux data versus energy and sector. The left-hand column plots (Figs. 1a–1c) are shown with a color scale that spans the observed dynamic range for the $E < 100$ eV energy interval. The altitudes and local times of these observations are listed above each plot. Note that the observations were made during 3 completely different orbits in the summer of 2004. The right-hand column plots (Figs. 1d–1f) show the same data, but with a color scale that highlights the photoelectron observations. The photoelectrons are identified with the green-blue peaks in the 10–20 eV range in sectors 2–5. The monotonically decreasing spectra seen in sectors 7 through 15 are thought to be either shocked solar wind electrons or spacecraft-emitted photoelectrons.

Fig. 2 presents energy spectra for the same observation points. Three energy spectra are shown in each plot (for sectors 1, 3, and 6). It is seen that the sector 3 spectra are different from the other two. The peaks at 15 and at 20 eV are clearly defined. Because the primary electrons from photoionization of the Mars upper atmosphere from the HeII 30.4 nm solar line should be located at 23 and 28 eV, the shift implies a spacecraft potential of roughly 8 V negative.

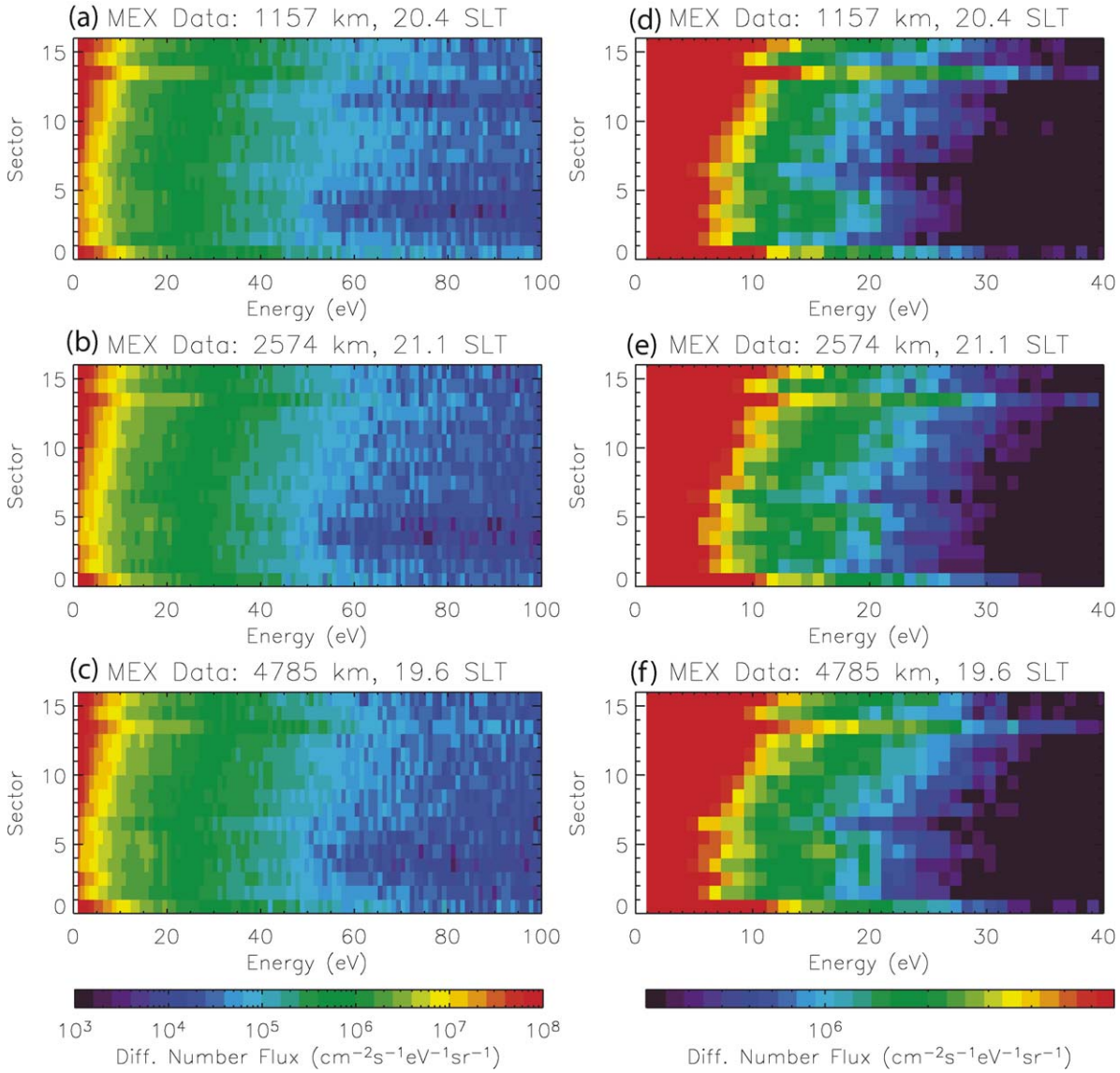


Fig. 1. Mars Express ASPERA-3 Electron Spectrometer data at 3 example locations containing high-altitude photoelectron signatures. Shown are differential number fluxes as a function of energy (in eV) and anode sector (0–15). The altitudes are (a) 1200, (b) 2600, and (c) 4800 km. The left-hand column (a–c) share a color scale that spans the observed dynamic range of the $E < 100$ eV electron fluxes. The right-hand column (d–f) are the same data but with a different color scale that highlights the atmospheric photoelectrons. The signatures of interest are the two peaks near 15 and 20 eV in sectors 2–5.

It is useful to compare the high-altitude photoelectron observations with the low-altitude photoelectron observations from ASPERA-3. An sample plot of ELS data taken at periapsis (near 300 km altitude) is presented in Fig. 3. The same features are seen in Fig. 3 as in Fig. 2, namely the primary photoelectron peaks near 20 eV. Note that the peaks show slightly higher energies at 300 km than are shown by those at high altitudes, with the lower peak at around 17–19 eV and the upper peak near 22–24 eV. Thus, it can be deduced that the spacecraft potential is only 4–6 V negative at this altitude. Furthermore, it appears that the potential is slightly different depending on the flight path of the electrons near the spacecraft (i.e., it is different for different sectors). The similarity between the 15–25 eV range of sector 3 in Fig. 2 with the corresponding range in Fig. 3 implies that the high-altitude observations may represent atmospheric photoelectrons.

Observations of atmospheric photoelectrons at thousands of kilometers above the planet are observed near the magnetosheath flanks. Frahm et al. (2006) (this issue) shows a record of atmospheric photoelectrons at 10,000 km in the tail of Mars. The normal situation is that such electrons are observed on seemingly random orbits over at least a brief interval. They usually come and go throughout the outbound leg along the dusk flank of Mars. The duskside preference mentioned is likely to reflect a sampling bias, but this has not been confirmed. A complete statistical survey of these photoelectrons is not, however, the point of this study and thus deferred to the future. This discussion provided here is only to demonstrate the

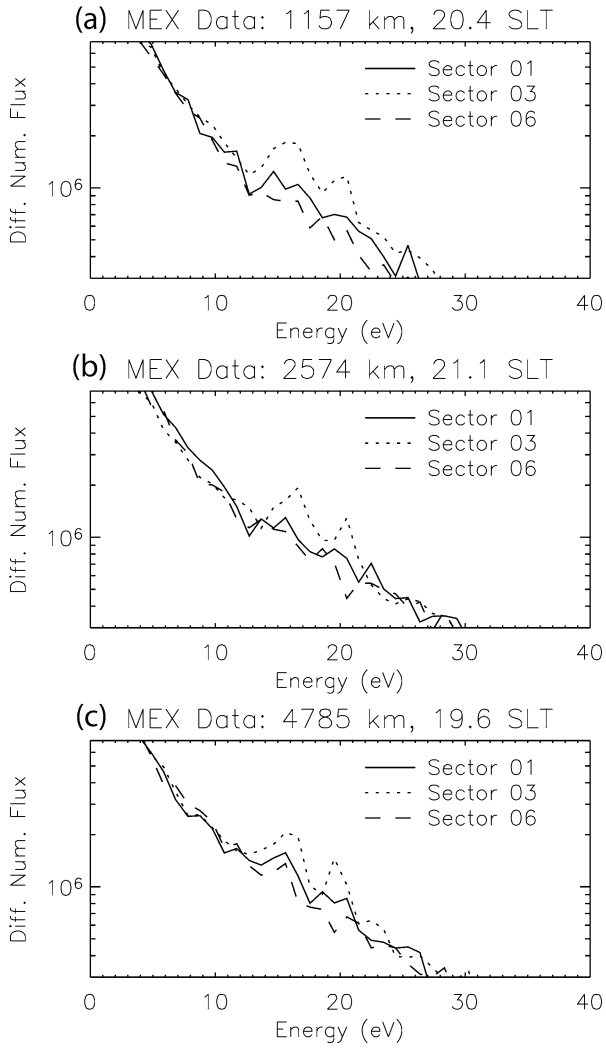


Fig. 2. Observed energy spectra from sectors 1, 3, and 6 for the 3 example observations presented in Fig. 1.

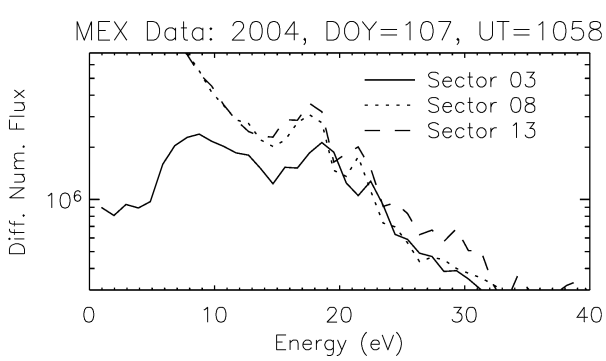


Fig. 3. Example atmospheric photoelectron data from a low-altitude (∼300 km) observation by ELS.

common occurrence of high-altitude atmospheric photoelectrons.

## 3. Magnetic field line modeling

The purpose of the present investigation is to interpret the high-altitude photoelectrons through the use of two numerical tools. The first is a global magnetohydrodynamic (MHD) model that solves for the bulk plasma parameters everywhere in the vicinity of Mars (Ma et al., 2002, 2004). The model solves the dimensionless conservative form of the MHD equations using multiple continuity equations (with separate solutions for the mass densities of $H^+$, $O^+$, $O_2^+$, and $CO_2^+$) but with single-fluid (that is, combined) momentum and energy equations. The magnetic field is also calculated self-consistently with the plasma solution. The fluid equations are solved by means of a sophisticated, second-order accurate, numerical scheme (Powell et al., 1999). The MHD model is combined via one-way coupling with the Mars Thermospheric General Circulation Model (MTGCM) of Bougher et al. (2001) for a realistically specified upper atmosphere (although there is no feedback to the MTGCM from the MHD code). Numerous chemical reactions are considered in the calculation to allow an accurate representation of the sources and sinks for each ion species. Mars, of course, has strong magnetic field sources in its crust (Acuña et al., 1999), which are taken into account by using the spherical harmonic crustal magnetic field model of Arkani-Hamed (2001, 2002).

The presently-adopted version of this code uses a spherical grid, allowing for a closely-spaced array in altitude and a larger spacing of grid cells in latitude and longitude. The radial resolution is 10 km from 100 to 600 km altitude, and it then expands to nearly a martian radius out in the unperturbed solar wind. The angular resolution is 1.875° to 3.75°.

Upstream and planetary boundary conditions are held constant and the model is run until a steady state solution is achieved. For the simulation presented here, the upstream solar wind conditions are as follows: the density is set at 4 $cm^{-3}$, the bulk speed is set at 400 $km\,s^{-1}$, the temperature is set to $3 \times 10^5$ K for the electrons and $5 \times 10^4$ for the ions, and the interplanetary magnetic field is set to 3 nT in magnitude completely in the $x$–$y$ plane at a nominal Parker spiral angle (56°) to the solar wind flow. The planet rotational axis is aligned with the $z$-axis of the simulation with a subsolar longitude of 180°. This means that the region of strong crustal fields is roughly pointed at the Sun. These are all reasonable values for the solar wind environment around Mars (Luhmann and Brace, 1991). See also Ma et al. (2002, 2004) for further details concerning the computational scheme and simulation set up used in this study.

Fig. 4 presents MHD results for the steady-state simulation described above. The color shows the magnetic field magnitude in the $x$–$z$ plane and also at the inner boundary of the simulation (that is, at 100 km altitude), and the white mesh shows the grid on the inner boundary. The three lines show the magnetic field lines through the locations of the 3 selected photoelectron observations illustrated in Fig. 1. The small square along each line shows the exact location of the measurement along each field line. The purple, white, and blue lines pass through the 1200, 2600, and 4800 km altitude observations, respectively.

The major result of Fig. 4 is that two of the three magnetic field lines connect to the planet's surface. They connect to Mars in very different places, but both of these field lines are definitely aligned downward toward the surface at the 100 km

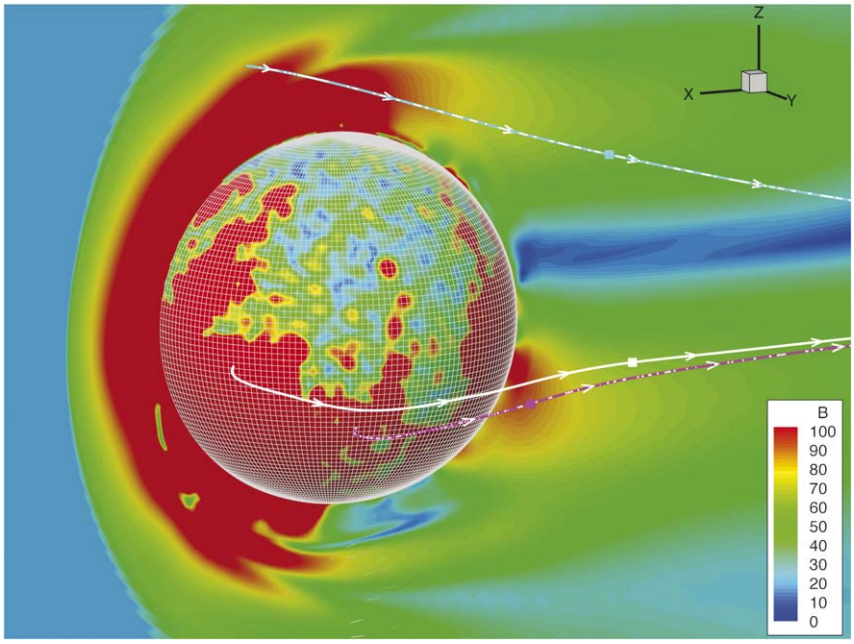


Fig. 4. Steady-state MHD simulation results for nominal solar flux and solar wind conditions. The color scale shows the magnetic field amplitude in the $x$–$z$ plane and also on the inner boundary surface of the simulation domain (at 100 km altitude). The white mesh shows the grid resolution on the inner boundary. The three lines are extracted field lines that pass through the locations of the 3 example observations presented in Fig. 1. The purple/pink line passes through the 1200 km observation location, the white line passes through the 2600 km altitude observation location, and the blue/cyan line passes through the 4800 km altitude observation location.

altitude inner boundary of the simulation domain. The field line for the lower altitude observation (at 1200 km, the purple line) connects near dusk while the field line for the higher altitude observation (at 2600 km, the white line) connects in the early afternoon. Note that the real subsolar longitudes at the time of these two examples are 219° and 160°, respectively (the 1200 km observation was made at 19:57 UT on day 187 of 2004 and the 2600 km observation was made at 04:09 UT on day 156 of 2004). Therefore, the planetary configuration in the simulation, with the strong crustal field sources rotated toward the Sun, is essentially correct for these two examples. We are thus reasonably confident that the atmospheric photoelectrons were observed along open magnetic field lines (that is, field lines connected both to the planet and to the interplanetary magnetic field).

The third example for the observation taken at 4800 km altitude (i.e., at a higher latitude than the other two examples) is on a field line trace that does not come particularly close to the planet. In fact, in this simulation, the field line traces through the magnetosheath, attaining a closest approach of ∼1800 km to the planet's surface. The extracted field line is well above the induced magnetospheric boundary (IMB), which is the altitude where the solar wind observations essentially disappear and the plasma observations become dominated by the ionospheric populations (Lundin et al., 2004). Clearly, this is not a field line that should be populated by atmospheric photoelectrons. For this observation, however, the subsolar longitude was 51°, not the 180° used in the simulation (the observation was made at 19:09 UT on day 166 of 2004). Therefore, the real topology could, for this case, be drastically different from that of the extracted field line. There are many other factors that also could lead to a data-model discrepancy, most notably the solar wind and interplanetary magnetic field conditions during the orbit. Because this is a northern hemisphere observation, it most likely that the field line was not open but, rather, draped (like the blue one in Fig. 4), but crossing below the IMB into the ionosphere at some point. Therefore, it is concluded that not all high-altitude photoelectron observations are on open field lines, but that some can occur along draped field lines as well.

Fig. 5 shows a few relevant parameters for one of the field lines (specifically, the white line in Fig. 4 through the 2600 km altitude observation). The three quantities of altitude, solar zenith angle, and magnetic field magnitude are plotted as a function of distance along the field line in Figs. 5a, 5b, and 5c, respectively. Also shown in Fig. 5d is the step size along the field line taken in the kinetic simulations, to be discussed in the next section. The magnetic field varies from nearly 300 nT in the ionosphere to roughly 10 nT at 2600 km altitude where the observation was made (at ∼8000 km distance along the field line). The magnetic field through the 1200 km altitude sample observation is quite similar to this one and will not be shown.

Fig. 6 is similar to Fig. 5 but it shows the parameters along the draped magnetic field line (the blue line from Fig. 4 through the 4800 km altitude observation). In Fig. 6a, the solid curve shows the values extracted from the MHD simulation results, while the dotted line is the same altitude profile shifted downward until the closest approach is at 200 km. It was lowered so that atmospheric photoelectrons would be produced in the flux tube, and therefore results from a draped field line passing through the magnetic pile-up region could be presented. It is this lowered version of the field line that will be used in the ki-

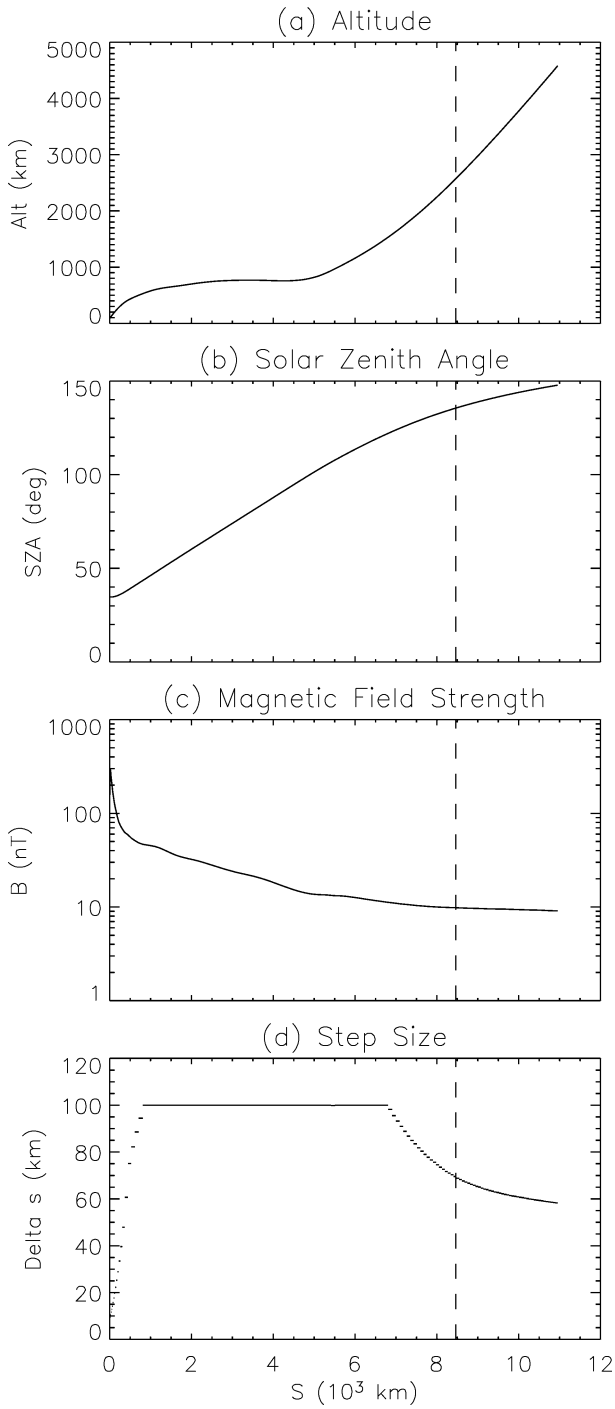


Fig. 5. Several quantities describing the extracted magnetic field that passes through the 2600 km altitude observation location (early afternoon ionospheric footpoint). Shown are (a) altitude, (b) solar zenith angle, (c) magnetic field magnitude, and (d) step size used in the kinetic simulation. All quantities are shown as a function of distance along the field line. The vertical dashed lines show the location of the observation along this field line.

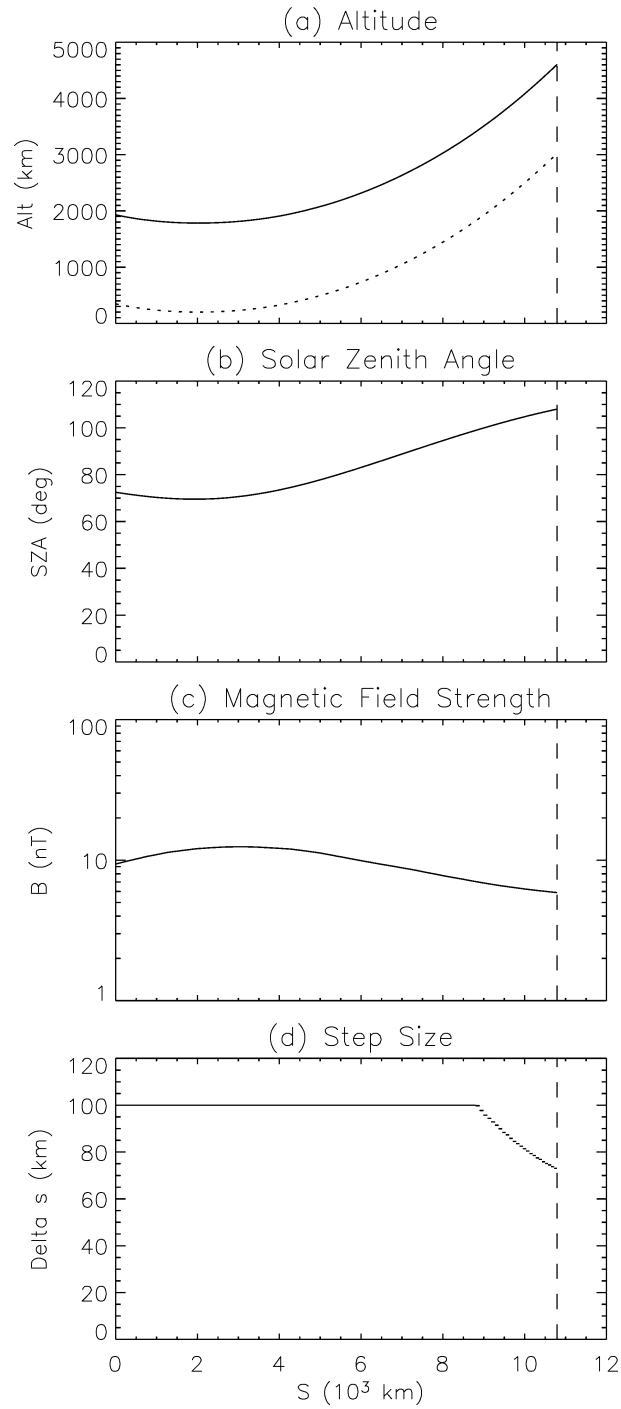


Fig. 6. Like Fig. 5 except for the extracted magnetic field line that passes through the 4800 km altitude observation location (draped IMF field line). The dotted line in (a) shows the downward-shifted altitude dependence of the field line that was used in the kinetic model simulations.

netic simulations discussed below. This, of course, means that the field line no longer passes through the observation point, but this is not a critical obstacle to the analysis. The only thing needed to demonstrate the concept of magnetic connectivity for these atmospheric photoelectron measurements is for the field line to pass close to the planet and then veer to higher altitudes. This issue of field line specification will be discussed again in the next two sections.

There are many similarities between the open field line plotted in Fig. 5 and the draped field line plotted in Fig. 6, but there are also some important differences. One similarity is that the closest approach to Mars is coincident with the location of the smallest solar zenith angle. This means that the photoelectron source along the field line is dominated by this

closest approach location, and the extra ambiguity of multiple source regions is avoided. The second similarity is that the magnetic field strength reaches its maximum value at this location as well. This means that there should be a well-defined source cone in the pitch angle distribution, allowing for a distinct mapping back to this source region. The third similarity is that the observations are thousands of kilometers away from this source region. Most of that distance, however, is above the thermosphere and ionosphere, so collisional scattering and degradation of the velocity space distribution should not be significant.

A clear difference between the field lines is in the magnetic field strength, particularly at the source region. The open field line, which is connected to the crustal field sources of Mars, has a maximum of nearly 300 nT while the draped IMF line only reaches 12 nT. Comparing this to the values at the observation locations along each field line (10 and 6 nT, respectively), the magnetic field ratios are dramatically different between these two field lines. This translates to vastly different source cone widths in pitch angle, which vary as the square root of one minus the B-field ratio.

Because the draped field line has been artificially lowered to a closest approach of 200 km, the B-field profile could be significantly different. That is, because the extracted field line is always above the IMB, it never crosses through the magnetic pile-up region, which often has a peak much higher than 12 nT (e.g., Crider et al., 2000, 2002; Vennerstrom et al., 2003). Let us reiterate that this is not a critical obstacle to the analysis, and in fact is useful in demonstrating the applicability of these results.

The fact that two of the three case studies are predicted to be on open field lines is actually unusual. Most nightside observations on field lines associated with the Mars crustal magnetic anomalies show either downflowing solar wind electrons or plasma voids (e.g., Mitchell et al., 2001; Lillis et al., 2004; Soobiah et al., 2006, this issue). These other studies, however, examined low-altitude data (at a few hundred km altitude), where the field lines most likely connected to the planet on the nightside. The field lines in the present study, however, connect to the dayside of Mars, and therefore are populated by freshly-generated atmospheric photoelectrons.

## 4. Photoelectron modeling

In order to simulate the electron distribution along the selected field lines, a numerical tool that includes the effects of the magnetic inhomogeneity along the field line should be employed. The model used here is a kinetic transport code for superthermal electrons developed for the Earth space environment (Khazanov et al., 1993, 1994; Khazanov and Liemohn, 1995; Liemohn et al., 1997). It has recently been modified for calculations of the Mars space environment (Liemohn et al., 2003). It simulates hot electron transport along a flux tube by calculating the time-dependent superthermal electron distribution function, $f$, from the gyration-averaged kinetic equation (e.g., Khazanov et al., 1994; Liemohn et al., 1997, 2003), as a function of time, distance along the field line, particle energy, and cosine of the pitch angle at the minimum B-field location. The inhomogeneity of the geomagnetic field, B, is included, as well as other forces, such as parallel electric fields (which, however, are assumed to be zero in this calculation). Superthermal electron sources are included in the equation, with the solar flux spectrum calculated from the Hinteregger et al. (1981) model as scaled by an F10.7 value interpolated from the Earth's F10.7 time series, taking into account the Earth–Sun–Mars angle (and a Sun–Mars distance scaling factor). The correction proposed by Solomon et al. (2001) is also applied, which quadruples the flux of photons for wavelengths below 20 nm. All of the simulations presented below have the same F10.7 value applied to them; namely an average value at Mars for the summer of 2004. This is justified because of the uncertainties associated with interpolating the F10.7 value from the Earth and the use of an empirical model spectrum. Note that Auger electron production is included in the source term. A collection of collision integrals are also included, which, in the present calculation, means interactions with thermal electrons and ions, elastic scattering with neutral particles, and inelastic excitation and ionization scattering with neutral particles. The neutral atmosphere and background ionosphere are specified from the MTGCM, consistent with the MHD simulations. The model uses the numerical technique of Khazanov et al. (1984, 1994), which replaces the derivatives with second-order accurate advection and diffusion schemes. The generality of the background magnetic field allows for the calculation of open field line transport as well as closed field line plasma motion. Liemohn et al. (2003) used this code to simulate and interpret Mars Global Surveyor observations of atmospheric photoelectrons along closed crustal field lines. See Khazanov et al. (1994), Khazanov and Liemohn (1995) and Liemohn et al. (1997, 2003) for further details of this code.

In the simulations for the present study, the energy step was held fixed at 1 eV for the range 0.5–200.5 eV. The pitch angle step size is a uniform 3° at the location of minimum B-field along each field line. The local pitch angle grid for any other point along the field line comprised of a mapping of this uniform grid to that location according to the magnetic field ratio. The spatial step size along the field line varied from 5 km at the lowest altitudes (∼100 km) up to a maximum step size of 100 km. It was also limited so that the change in vertical position was less than the smallest local scale height for the plasma or neutral species. Thus the 100 km step sizes seen in Fig. 6 near the closest approach of the field line (that is, at 200 km altitude) are believed to be acceptable because the field line changes altitude very slowly in this region. That is, even though the plasma scale heights at 200 km altitude are between 20 and 30 km (Hanson et al., 1977), the 100 km step size in the kinetic simulation at this location translates to less than 10 km of vertical step size because the field line is nearly horizontal.

Note that these electrons travel very fast along the field line, and thus a steady state simulation justified. For example, a 25 eV electron is moving 3000 km/s, nearly 1 $R_M$/s. Because the magnetic field topology focuses the electrons into a source cone distribution, most of their velocity is field-aligned. So, they reach the observation altitudes within a few seconds,

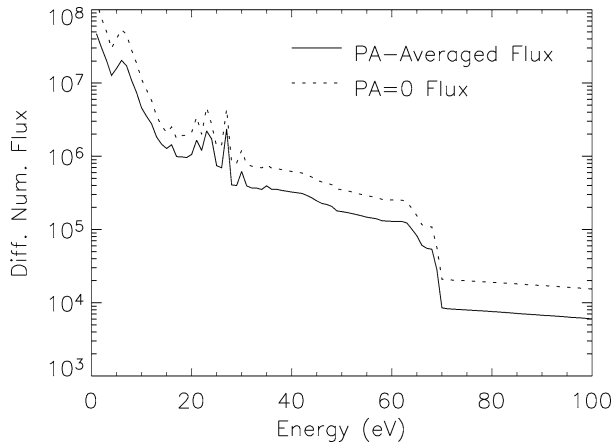


Fig. 7. Example low-altitude atmospheric photoelectron results from the kinetic model. These are at 200 km altitude along the field line shown in Fig. 5. The solid line is the pitch angle averaged energy spectrum and the dotted line is the energy spectrum at $\alpha = 0$.

and so even mV/m convective electric fields (e.g., Kallio and Janhunen, 2002; Vennerstrom et al., 2003) will not cause much cross-field drift.

Each of the three field lines was used for the magnetic field in the kinetic model simulation. For reference and validation, Fig. 7 presents low-altitude (ionospheric) photoelectron energy spectra from one of the simulations (at 200 km altitude along the "early afternoon" open field line in Fig. 4, shown in white). Two spectra are presented: the pitch angle averaged spectrum and the spectrum at zero pitch angle. The primary photoelectron peaks are clearly seen in the 20–30 eV range, as well as a dip near 4 eV caused by vibrational excitation. The "knee" at 70 eV is due a sharp decrease in the solar flux ultraviolet spectrum near 16 nm. All of these features are standard atmospheric photoelectron signatures seen at Earth (e.g., Nagy and Banks, 1970; Doering et al., 1976; Winningham et al., 1989; Khazanov and Liemohn, 1995, 1998) and previously modeled for the martian ionosphere (Mantas and Hanson, 1979; Fox and Dalgarno, 1979; Liemohn et al., 2003). Note that there are many primary photoelectron peaks in the 20–30 eV range, but the 2 largest are at 23 and 28 eV. The difference between the two energy spectra is a reflection of the fact that the upward fluxes are larger than the downward fluxes, as expected because there is no photoelectron source anywhere else along the field line.

Fig. 8 shows high-altitude results from the three sample field lines. Figs. 8a–8d show results at 1200 km altitude along all three field lines, while Figs. 8e–8h show results at the "top" of each field line, at its particular altitude (4800 km for the two open field lines and 3100 km for the draped field line). Figs. 8a and 8e show energy spectra from the three simulations at zero pitch angle, while the other panels in Fig. 8 show color plots of the differential number flux versus energy and pitch angle (similar to Fig. 1).

There is little difference between the results at 1200 km and those at the top of the simulation domain. The main difference is that the fluxes are lower at higher altitude as the electrons undergo a few collisions along the field line. This is true mainly for the very lowest energy electrons (below ∼10 eV). These collisions also cause some pitch angle scattering, as evidenced by the spreading of the distribution beyond the source cone at low energies (again, this is most noticeable below 10 eV). Note that the topside boundary condition is that no electrons are flowing down the field line at this point. This was done in order to isolate the photoelectron signature, and not mix it with the precipitating (and potentially backscattered) solar wind electrons. Therefore, the pitch angle distribution between 90° and 180° is completely empty in the "top" column and close to empty at 1200 km altitude.

It is noteworthy that the collisional effects on the velocity space distribution of the photoelectrons are limited to energies below 10 eV. This means that the primary photoelectron peaks in the 20–30 eV range are pristinely preserved along the entire extent of the field line. Therefore, if a sensitive detector were to cross one of these field lines, it should observe discernible photoelectron peaks. This is exactly the case with the ASPERA-3 ELS instrument on board Mars Express.

## 5. Data-model comparisons

Let us begin this analysis by making a qualitative comparison between the ASPERA-3 observations of photoelectrons and the simulation results for this phenomenon. This will then be followed by a more rigorous quantitative comparison between the electron fluxes. The section concludes with a description of how to extract magnetic field information from these high-altitude atmospheric photoelectron observations.

### *5.1. Low-altitude comparison*

For the low-altitude data-model comparison, it is seen that the observed flux peak (in Fig. 3) within the primary photoelectron peaks (15–25 eV) is just over $3 \times 10^6$ (eV cm$^2$ s sr)$^{-1}$, while the simulated flux peak (Fig. 7) in this energy range is around $5 \times 10^6$ (eV cm$^2$ s sr)$^{-1}$. This is quite close, and, after the energy shift due to spacecraft charging is taken into account, the shapes of the observed and modeled spectra are very similar (there is more detail in the model results because of the finer energy resolution). The flux difference between them can be explained by the uncertainty in both the solar flux spectrum and a difference in ionospheric location. The first uncertainty exists because the solar flux spectrum was taken from an Earth-based empirical model with the scaling factor (F10.7) interpolated from Earth observations. The second uncertainty exists because the observations are from different solar zenith angles (Fig. 5b shows the simulated solar zenith angle to be 35° while the value for the observations was about 65°). Another difference is that the observations are at 300 km while the simulations are from 200 km.

One of the spectra in Fig. 3 (the data from sector 3) is substantially lower in flux than is the case in the other two channels. This is predicted by the model, as evidenced by the lower fluxes for the pitch-angle-averaged spectrum than from the $\alpha = 0$ spectrum. The effect is because the field line is connected to the ionosphere at only one point and the "downward

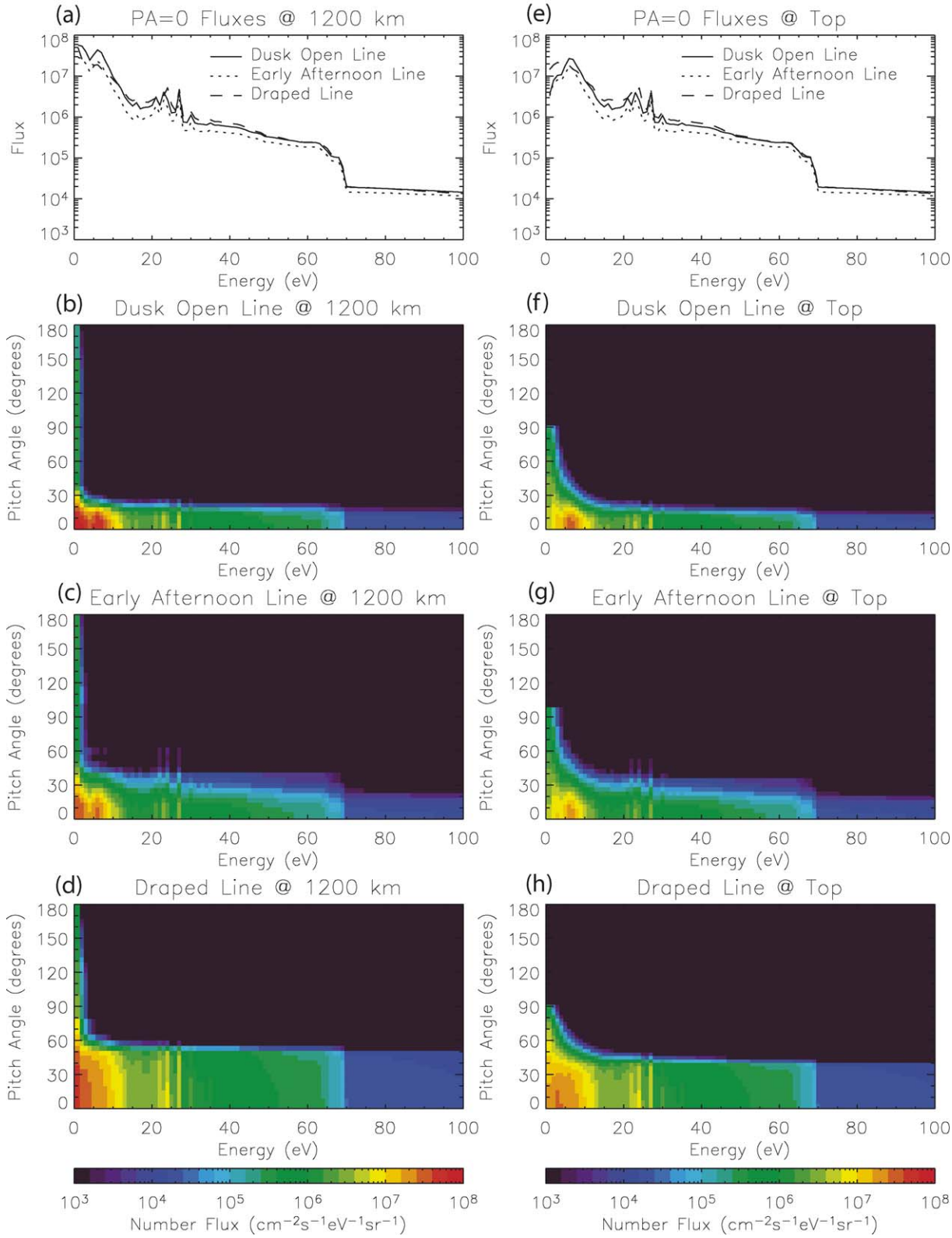


Fig. 8. High-altitude atmospheric photoelectron results from the kinetic model. The left-hand column, panels (a–d), show results at 1200 km altitude along each field line while the right-hand column, panels (e–h), show results at the top of each field line (near 4800 km altitude). The top row, panels (a) and (e), show $\alpha = 0$ energy spectra at these altitudes for the 3 field line configurations. The other 3 rows show differential number flux versus energy and pitch angle. All of the color plots share the same logarithmic color scale, the same one used for Figs. 1a–1c.

flowing" fluxes (pitch angles greater than 90°) are substantially lower than the upflowing fluxes. This hemispheric difference in the simulation results is seen in the measurements. Note that the very low energies (<10 eV) are substantially different in the

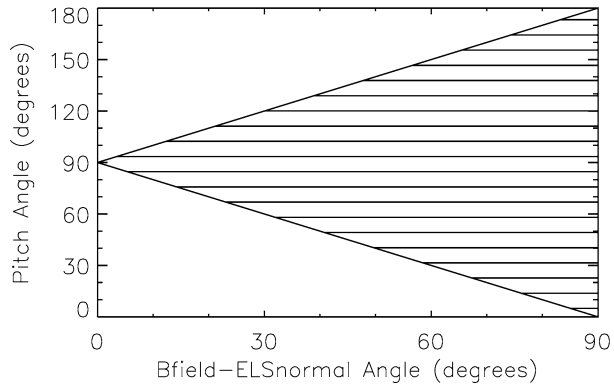


Fig. 9. Observed pitch angle extent as a function of the angle between the local magnetic field vector and the ELS normal vector.

spectra shown in Fig. 3. This is thought to be caused by spacecraft effects, but the true reason is unknown.

### 5.2. High-altitude comparison

The high-altitude observations (Figs. 1 and 2) all have peak flux values in the primary photoelectron peak energy range near $2 \times 10^6$ (eV cm$^2$ s sr)$^{-1}$. The simulations (Fig. 8), which are supposed to be along the same field lines, are higher, with a peak flux value in this energy range above $4 \times 10^6$ (eV cm$^2$ s sr)$^{-1}$. Again, this could be explained by the same uncertainties mentioned with respect to the low-altitude results, namely that the real solar flux spectrum is unknown and that the real ionospheric footpoint of these field lines is unknown. As in the case of the low-altitude comparison, the shapes of the observed and modeled spectra are quite similar (after the shift has been removed from the measured values). Thus, there seems to be good qualitative agreement between the data and the computational results.

The fact that the atmospheric photoelectrons are only seen in a few sectors of the ELS anode ring is actually a useful trait. Remember that there is no magnetic field measurement made on Mars Express, and thus the distribution across the anode sectors cannot readily be converted into a pitch angle distribution. In fact, the ELS will not usually see the entire pitch angle range from 0° to 180°, but rather a limited extent centered around 90° pitch angle. The relationship between the observed pitch angle range and the angle between the local magnetic field vector and the vector normal to the ELS anode ring is represented graphically in Fig. 9. When the two vectors are parallel, only the locally mirroring electrons are observed. When the two vectors are perpendicular, the entire pitch angle range is seen by the ELS. Note again (see above) that the ELS samples this pitch angle range twice. However, because the azimuthal angle of the local magnetic field vector with respect to sector zero is unknown, we do not know where to start the sector sequence within the observed pitch angle range. It transpires that there are many difficulties in extracting a magnetic field direction, let alone an amplitude, from such an instrument without the aid of a local magnetic field measurement.

Table 1
Data facts for the 3 example cases of high-altitude atmospheric photoelectrons

| Case | Altitude (km) | SLT (h) | Latitude (deg.) | PE data (# of sectors) | PE data peak sector | Peak offset from sector 3 (deg.) |
|---|---|---|---|---|---|---|
| 1 | 1200 | 20.4 | −16 | 3 | 3 | 0 |
| 2 | 2600 | 21.1 | 3 | 4 | 3 | 0 |
| 3 | 4800 | 19.6 | 29 | 5 | 4 | −23 |

### 5.3. High-altitude pitch angle comparison and magnetic field inference

This is where the limited sector extent of the atmospheric photoelectron observations becomes useful. From the Mars Express ephemeris data, the ELS normal vector as well as the look directions for each of the ELS anodes are known. Therefore, the direction in which photoelectrons are observed is known. From the MHD simulation results, the modeled local magnetic field vector is known. Finally, from the kinetic simulation results, the modeled pitch angle extent of the source cone is known. Putting all of this together, we know what ELS saw and what ELS should see if the simulation results are valid.

The main unit of the ASPERA-3 instrument, of which ELS is a component, is mounted near a "top corner" of the Mars Express spacecraft. The ELS detector plane is parallel to one of the "sides" of Mars Express. In orbit around Mars, the nominal operational configuration of ASPERA-3 has the ELS detector plane essentially parallel to the ecliptic plane, with sector 3 looking sunward and sector 7 looking toward dawn. For this study, the ELS normal vector is therefore assumed to be in the $+z$-axis direction in all three case studies.

Table 1 lists a few observational facts about the three example cases of high-altitude atmospheric photoelectron measurements. Given are the altitude, solar local time, and latitude of the position of the observations. The next column gives the number of anode sectors in which the photoelectron flux in the 15–20 eV range was greater than $10^6$ (eV cm$^2$ s sr)$^{-1}$. The next column lists the sector of the photoelectron flux peak. Because there are 16 sectors in the ring, each one has a viewing width of 22.5°. The final column in Table 1 uses this number to convert the sector of the peak into a quantitative azimuthal offset (in degrees) in the $x$–$y$ plane relative to the sunward direction. The non-zero offset for case 3 implies a non-zero B$y$ for the local magnetic field vector. In fact, the skew toward sector 4 (rather than sector 2) implies a B$y$ value of opposite sign to the B$x$ value.

For the three selected sample observations, the simulated magnetic field vectors are listed in Table 2. It is seen that the vectors for all three cases are primarily contained in the $x$–$y$ plane. That is, B$z$ is relatively small compared to the field intensity, which is also given. The fifth column of Table 2 lists the magnetic field ratio between the values at the observation location and the photoelectron source (lowest altitude of the field line). This magnetic field ratio translates into the values of the next column, which are the simulated source cone widths at the observation locations. Fig. 10 shows the relationship between these two quantities. Note that the simulated source cone widths are not the same as the electron pitch angle extents, because

Table 2
Simulated magnetic field values for the 3 example cases

| Case | B$x$ (nT) | B$y$ (nT) | B$z$ (nT) | \|B\| (nT) | B ratio local/source | Sim. source cone (deg.) | Sun–B angle (deg.) |
|---|---|---|---|---|---|---|---|
| 1 | −11.4 | 0.83 | 2.6 | 11.7 | 0.21 | 27 | −4 |
| 2 | −9.8 | 0.29 | 0.46 | 9.8 | 0.095 | 18 | −2 |
| 3 | −4.0 | 3.9 | −0.84 | 5.7 | 0.41 | 40 | −44 |

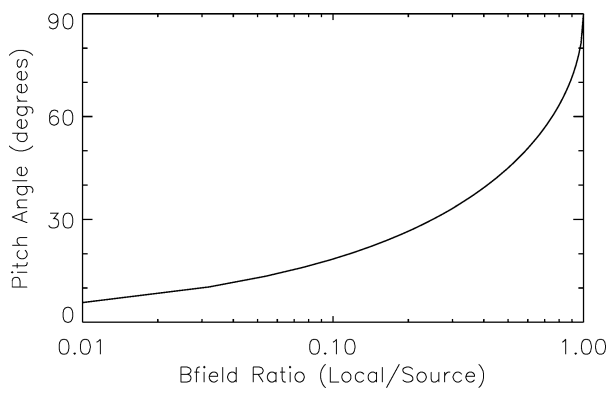


Fig. 10. Source cone pitch angle extent as a function of the ratio between the local magnetic field intensity and the intensity at the photoelectron source region.

scattering could broaden the electron distribution. Therefore, these widths are lower limits to the pitch angle extents (to be compared and discussed below).

The final column of Table 2 lists the angle in the $x$–$y$ plane of the magnetic field relative to the sunward direction. This column is directly comparable to the last column of Table 1. For cases 1 and 2, the simulated Sun–B angles are within a few degrees of zero, as was observed. For case 3, the simulation predicts a 44° offset, which is essentially 2 sector widths, while the ELS data only show a shift of 1 sector. The trend, however, is the same between the data and the simulation results (i.e., the magnetic field is flaring away from the $x$-axis). The inference to be made about the real magnetic field vector for case 3 is that the real field line is more anti-sunward and less flared than the simulated field line.

The simulated and observed pitch angle extents are listed in Table 3. The second column of Table 2 gives the simulated pitch angle extents of the primary photoelectron peaks (specifically, at 23 eV) at the observation locations. This value is slightly larger than the theoretical source cone width because of scattering (as well as numerical diffusion, which is thought to be small). As with the data, this extent is defined as the pitch angle at which the differential number flux drops below $10^6$. The error on numbers in this column is therefore only a few degrees, at most.

The third column of Table 3 is the inferred pitch angle extent of the atmospheric photoelectron observations. This was computed by dividing the number of sectors (listed in Table 1) in half, multiplying by 22.5°. The error in the inferred observed pitch angle extent is therefore at least 11° and could be more than a full sector width (that is, it can be off by a sector plus the ELS–B angle error). As seen in the table, the observed and simulated pitch angle extents are within error of each other for every case.

Table 3
Simulated and observed pitch angle extents of atmospheric photoelectrons

| Case | Sim. PA extent at 23 eV (deg.) | Min. obs. PA extent (deg.) | ELS–B angle (deg.) | Predicted obs. PA range (deg.) | Predicted obs. PA extent (deg.) |
|---|---|---|---|---|---|
| 1 | 30 | 34 | 77 | 13–167 | 47 |
| 2 | 40 | 45 | 87 | 3–177 | 48 |
| 3 | 47 | 57 | 81 | 9–171 | 66 |

Before discussing this further, let us continue presenting the numbers listed in Table 3. The next column gives the angle between ELS normal vector and the simulated local magnetic field vector. Because B$z$ is relatively small compared to |B| (listed in Table 2) in each case, these angles are all very large. Thus, if the simulated magnetic field is the true one, then this indicates that the ELS observed nearly all of the pitch angle distribution. The next column lists these "observed pitch angle ranges," as inferred from this analysis and taken from Fig. 9. The final column in Table 3 lists an inferred "real" pitch angle extent from the observations, taking into account the "unobserved" pitch angle range because of the B–ELS angle.

The simulated pitch angle extents are less than the observed extents in all three cases, with differences ranging from 4° to 10°. When the simulated magnetic field vector is taken into account, the differences increase to a range from 11° to 18°. This is within the errors of the calculations and observations, and shows that the model results are in reasonable agreement with the measurements. The differences between the observed and simulated pitch angle extents listed in Table 3 can be explained by a number of factors, most of them already mentioned in the sections above. In actuality, the details of these differences do not particularly matter, because the comparisons are close enough to justify the main conclusion of this study, namely that the high-altitude photoelectrons most likely originate in the dayside ionosphere, and reach the observation locations by traveling along magnetic field lines that connect the two points. In addition, the connecting field lines can be either draped IMF lines or open field lines (connected to the planet and to the IMF).

The method described in this section, of identifying and interpreting high-altitude atmospheric photoelectron observations, can be used to infer a magnetic field direction from the ELS data. The technique is similar to those used with Mars Global Surveyor electron reflectometer data (Mitchell et al., 2001; Lillis et al., 2004). If the photoelectron observations are centered away from sector 3, then the magnetic field angle with respect to the Sun–Mars line can be determined. In addition, the extent of the photoelectrons across the sectors provides information about two quantities: the magnetic field ratio and the ELS–B field angle. When the observations are coupled with a global simulation of the magnetic field topology around Mars and/or a kinetic simulation of the photoelectron distribution, the extracted information becomes even greater.

## 6. Conclusions

In this study, two numerical models were used to analyze the characteristics of the high-altitude atmospheric photoelectron measurements from ASPERA-3 reported by Frahm et al. (2006) (this issue). One model is a global MHD code (Ma et al., 2002, 2004). Field lines were extracted from a steady-state simulation output produced with regard to nominal solar flux and solar wind conditions. Two of the three field lines connected to the planetary crustal magnetic field source regions, while the third observation was along a draped interplanetary magnetic field line.

The other model is a kinetic transport model that simulates the electron distribution along a magnetic field line (Khazanov and Liemohn, 1995; Liemohn et al., 2003). It predicts that the photoelectrons above the inferred magnetospheric boundary are essentially confined to pitch angles within the source cone region of velocity space. This pitch angle extent is different for each field line, but ranged from 18° to 40° for the three sample observations studied here.

Using the known orientation of the ELS component of ASPERA-3 and the simulated magnetic field topology, an inferred pitch angle extent for the atmospheric photoelectron observations was derived. Reasonable agreement is shown between the data and the model results. While the simulated pitch angle extents are smaller than those inferred from the observations, the differences are within the uncertainty of the estimation. In addition, the sector of the photoelectron flux peak is a function of the magnetic field azimuthal angle in the detector plane. Agreement (within error) was shown between the observed and simulated azimuthal angles. A method was then demonstrated for inferring properties of the local and photoelectron source region magnetic field from the ELS measurements.

## Acknowledgments

The Michigan authors would like to thank support for this research by NASA under Grants NAG5-10887, NNG04G055G, and NAG5-13332, by the NSF under Grant ATM-0455729, and by subcontract from Southwest Research Institute under NASW-00003. The ASPERA-3 experiment on the European Space Agency (ESA) Mars Express mission is a joint effort between 15 laboratories in 10 countries, all sponsored by their national agencies. We thank all these agencies as well as the various departments/institutes hosting these efforts. We also wish to acknowledge the Swedish National Space Board for their support of the main PI-institute and we are indebted to ESA for their courage in embarking on the Mars Express program, the first ESA mission to the Red Planet.

## References

Acuña, M.H., and 12 colleagues, 1999. Global distribution of crustal magnetization discovered by the Mars Global Surveyor MAG/ER experiment. Science 284, 790–793.

Arkani-Hamed, J., 2001. A 50-degree spherical harmonic model of the magnetic field of Mars. J. Geophys. Res. 106, 23197–23208.

Arkani-Hamed, J., 2002. An improved 50-degree spherical harmonic model of the magnetic field of Mars derived from both high-latitude and low-latitude data. J. Geophys. Res. 107 (E10), doi:10.1029/2001JE001835. 5083.

Barabash, S., and 43 colleagues, 2004. ASPERA-3: Analyzer of space plasmas and energetic ions for Mars Express. In: Wilson, A. (Ed.), Mars Express: The Scientific Payload, ESA SP-1240. European Space Agency Publications Division, European Space Research and Technology Centre, Noordwijk, The Netherlands, pp. 121–139.

Bougher, S.W., Engel, S., Hinson, D.P., Forbes, J.M., 2001. Mars Global Surveyor Radio Science electron density profiles: Neutral atmosphere implications. Geophys. Res. Lett. 28, 3091–3094.

Chicarro, A., Martin, P., Trautner, R., 2004. The Mars Express mission: An overview. In: Wilson, A. (Ed.), Mars Express: The Scientific Payload, ESA SP-1240. European Space Agency Publications Division, European Space Research and Technology Centre, Noordwijk, The Netherlands, pp. 3–13.

Crider, D.H., and 12 colleagues, 2000. Evidence of electron impact ionization in the magnetic pileup boundary of Mars. Geophys. Res. Lett. 27, 45–48.

Crider, D.H., and 18 colleagues, 2002. Observations of the latitude dependence of the location of the martian magnetic pileup boundary. Geophys. Res. Lett. 29 (8), doi:10.1029/2001GL013860. 1170.

Doering, J.P., Peterson, W.K., Bostrom, C.O., Potemra, T.A., 1976. High resolution daytime photoelectron energy spectra from AE-E. Geophys. Res. Lett. 3, 129–131.

Fox, J.L., Dalgarno, A., 1979. Electron energy deposition in carbon dioxide. Planet. Space Sci. 27, 491–502.

Frahm , R.A., and 42 colleagues, 2006. Carbon dioxide photoelectron energy peaks at Mars. Icarus 182, 371–382.

Hanson, W.B., Sanatani, S., Zuccaro, D.R., 1977. The martian ionosphere as observed by the Viking retarding potential analyzers. J. Geophys. Res. 82, 4351–4363.

Hinteregger, H.E., Fukui, K., Gilson, B.R., 1981. Observational reference, and model data on solar EUV, from measurements on AE-E. Geophys. Res. Lett. 8, 1147–1150.

Kallio, E., Janhunen, P., 2002. Ion escape from Mars in a quasi-neutral hybrid model. J. Geosphys. Res. 107 (A3), doi:10.1029/2001JA000090. 1035.

Khazanov, G.V., Liemohn, M.W., 1995. Non-steady-state ionosphere–plasmasphere coupling of superthermal electrons. J. Geophys. Res. 100, 9669–9681.

Khazanov, G.V., Liemohn, M.W., 1998. Comparison of photoelectron theory against observations. In: Horwitz, J.L., Gallagher, D.L., Peterson, W.K. (Eds.), Geospace Mass and Energy Flow. In: Geophys. Monogr. Ser., vol. 104. AGU, Washington, DC, pp. 333–341.

Khazanov, G.V., Koen, M.A., Konikov, V.Yu., Sidorov, I.M., 1984. Simulation of ionosphere–plasmasphere coupling taking into account ion inertia and temperature anisotropy. Planet. Space Sci. 32, 585–598.

Khazanov, G.V., Liemohn, M.W., Gombosi, T.I., Nagy, A.F., 1993. Non-steady-state transport of superthermal electrons in the plasmasphere. Geophys. Res. Lett. 20, 2821–2824.

Khazanov, G.V., Neubert, T., Gefan, G.D., 1994. A unified theory of ionosphere–plasmasphere transport of suprathermal electrons. IEEE Trans. Plasma Sci. 22, 187–198.

Liemohn, M.W., Khazanov, G.V., Moore, T.E., Guiter, S.M., 1997. Self-consistent superthermal electron effects on plasmaspheric refilling. J. Geophys. Res. 102, 7523–7536.

Liemohn, M.W., Mitchell, D.L., Nagy, A.F., Fox, J.L., Reimer, T.W., Ma, Y., 2003. Comparisons of electron fluxes measured in the crustal fields at Mars by the MGS MAG/ER instrument with a B-field dependent transport code. J. Geophys. Res. 108, doi:10.1029/2003JE002158. 5134.

Lillis, R.J., Mitchell, D.L., Lin, R.P., Connerney, J.E.P., Acuña, M.H., 2004. Mapping crustal magnetic fields at Mars using electron reflectometry. Geophys. Res. Lett. 31, doi:10.1029/2004GL020189. L15702.

Luhmann, J.G., Brace, L.H., 1991. Near-Mars space. Rev. Geophys. 29, 121–140.

Lundin, R., and 44 colleagues, 2004. Solar wind-induced atmospheric erosion at Mars: First results from ASPERA-3 on Mars Express. Science 305, 1933–1936.

Ma, Y., Nagy, A.F., Hansen, K.C., DeZeeuw, D.L., Gombosi, T.I., 2002. Three-dimensional multispecies MHD studies of the solar wind interaction

with Mars in the presence of crustal fields. J. Geophys. Res. 107 (A10), doi:10.1029/2002JA009293. 1282.

Ma, Y., Nagy, A.F., Sokolov, I.V., Hansen, K.C., 2004. Three-dimensional, multispecies, high spatial resolution MHD studies of the solar wind interaction with Mars. J. Geophys. Res. 109, doi:10.1029/2003JA010367. A07211.

Mantas, G.P., Hanson, W.B., 1979. Photoelectron fluxes in the martian ionosphere. J. Geophys. Res. 84, 369–385.

Mitchell, D.L., Lin, R.P., Reme, H., Crider, D.H., Cloutier, P.A., Connerney, J.E.P., Acuña, M.H., Ness, N.F., 2000. Oxygen Auger electrons observed in Mars' ionosphere. Geophys. Res. Lett. 27, 1871–1874.

Mitchell, D.L., Lin, R.P., Mazelle, C., Reme, H., Cloutier, P.A., Connerney, J.E.P., Acuña, M.H., Ness, N.F., 2001. Probing Mars' crustal magnetic field and ionosphere with the MGS electron reflectometer. J. Geophys. Res. 106 (E10), 23419–23427.

Nagy, A.F., Banks, P.M., 1970. Photoelectron fluxes in the ionosphere. J. Geophys. Res. 75, 6260–6270.

Powell, K.G., Roe, P.L., Linde, T.J., Gombosi, T.I., De Zeeuw, D.L., 1999. A solution-adaptive upwind scheme for ideal magnetohydrodynamics. J. Comp. Phys. 153, 284–309.

Solomon, S.C., Bailey, S.M., Woods, T.N., 2001. Effect of solar soft X-rays on the lower ionosphere. Geophys. Res. Lett. 28, 2149–2152.

Soobiah, Y., and 42 colleagues, 2006. Observations of magnetic anomaly signatures in Mars Express ASPERA-3 ELS data. Icarus 182, 396–405.

Vennerstrom, S., Olsen, N., Purucker, M., Acuña, M.H., Cain, J.C., 2003. The magnetic field in the pile-up region at Mars, and its variation with the solar wind. Geophys. Res. Lett. 30 (7), doi:10.1029/2003GL016883. 1369.

Winningham, J.D., Decker, D.T., Kozyra, J.U., Jasperse, J.R., Nagy, A.F., 1989. Energetic (>60 eV) atmospheric photoelectrons. J. Geophys. Res. 94, 15335–15348.